Atmospheric Pollution Research 9 (2018) 584–593

HOSTED BY

Contents lists available at ScienceDirect

Atmospheric Pollution Research

journal homepage: www.elsevier.com/locate/apr

Investigation of air quality over the largest city in central China using high resolution satellite derived aerosol optical depth data

Kun Sun[a,*], Xiaoling Chen[a,b,**], Jialin Wang[a], Tianhao Zhang[a], Zhongmin Zhu[a,c]

[a] State Key Laboratory of Information Engineering in Surveying, Mapping and Remote Sensing, Wuhan University, Wuhan 430079, China
[b] The Key Laboratory of Poyang Lake Wetland and Watershed Research, Ministry of Education, Jiangxi Normal University, Nanchang 330022, China
[c] College of Information Science and Engineering, Wuchang Shouyi University, Wuhan 430064, China

ARTICLE INFO

Keywords:
Air pollution
Urban aerosol
Environmental monitoring
Aerosol optical depth
Wuhan

ABSTRACT

Urban air pollution in China has gained unprecedented attention under the background of high concentration of particulate matter and increasing haze frequency in recent years. In this study, utilizing the high resolution Aerosol Optical Depth (AOD) dataset derived from Gaofen-1 (GF-1) satellite during 2013–2016, we provide a new insight into the air quality over Wuhan, the largest city in central China. Local AOD (LAOD) was introduced to indicate the aerosol loading from local sources. Annual LAOD was found to increase with urban cover in the district scale, which revealed the potential positive feedback between urbanization and regional air pollution. The seasonal pattern of LAOD was consistent with $PM_{2.5}$, both presenting a seasonality of highest in winter and lowest in summer. By locating the highly polluted regions from LAOD map, our research highlighted the impact of anthropogenic aerosol loading (especially from industrial parks) on the regional air quality. Noticing the concentrated distribution of anthropogenic aerosol loading over urban areas, we further defined the urban-induced AOD to quantify the urban aerosol effect by comparing LAOD between urban areas and other land types. Consistent with the change trend of $PM_{2.5}$, annual urban-induced AOD also presented a slight downward trend, which was a reasonable response to the stricter environment policies adopted by local government in recent years. Though carried out as a case study over Wuhan in central China, we believe that the findings presented here would promote the understanding of air pollution in most mega cities of China.

1. Introduction

Atmospheric aerosols, generated from natural sources (e.g. sea spray, dust storm, and forest fire) and anthropogenic sources (e.g. fossil fuel, biomass burning, traffic and industrial emission), play a crucial role in climate change, radiative forcing, visibility and air quality (Haywood and Boucher, 2000; Kaufman et al., 2002; Wang et al., 2009; Huang et al., 2014; Stocker, 2014). However, owing to a wide spatial and temporal variability in aerosol mass concentration, aerosol type and aerosol composition, atmospheric aerosol remains to be a dominant source of uncertainty in the understanding of global climate system (Mishchenko et al., 2007; Stocker, 2014).

A convenient and efficient way to quantify the characteristics of atmospheric aerosol spatially and temporally is satellite remote sensing (Yang et al., 2014). Although there still exist a certain degree of uncertainty, a number of satellite-based instruments, such as Moderate Resolution Imaging Spectrometer (MODIS) (Hsu et al., 2013; Levy et al., 2013), Advanced Very High Resolution Radiometer (AVHRR) (Mishchenko et al., 2003), Total Ozone Mapping Spectrometer (TOMS) (Torres et al., 2002), Multi-angle Imaging Spectro-Radiometer (MISR) (Kahn et al., 2010), and Visible Infrared Imaging Radiometer Suite (VIIRS) (Jackson et al., 2013), have provided massive aerosol related products at global scale over the past few decades. One significant aerosol optical property derived from satellite measurements is Aerosol Optical Depth (AOD), which is used to indicate the degree of light attenuation by aerosols through the observation path of atmosphere.

Satellite derived AOD products have been widely used in the global/regional air quality study, including analyzing the formation of haze pollution (Tao et al., 2012, 2016), evaluating anthropogenic aerosol loading (Ginoux et al., 2010; Hao et al., 2011), and estimating the spatiotemporal distribution of $PM_{2.5}$ (Sorekhamer et al., 2013; Van Donkelaar et al., 2016). Nevertheless, most of the frequently-used AOD

Peer review under responsibility of Turkish National Committee for Air Pollution Research and Control.
* Corresponding author.
** Corresponding author. State Key Laboratory of Information Engineering in Surveying, Mapping and Remote Sensing (LIESMARS), Wuhan University, Wuhan, Hubei Province 430079, China.
E-mail addresses: sunkun@whu.edu.cn (K. Sun), Xiaoling_chen@whu.edu.cn (X. Chen).

https://doi.org/10.1016/j.apr.2017.12.011
Received 15 August 2017; Received in revised form 17 December 2017; Accepted 20 December 2017
Available online 29 December 2017

products at global scale (e.g. MODIS, AVHRR, MISR and VIIRS) have a spatial resolution ranging from a few kilometers to several tens of kilometers, which are too coarse to the urban scale applications. Take Wuhan, the largest city in central China for example, there only have 15 × 15 pixels at most covering the city for the commonly used MODIS AOD product at 10 km resolution. It is obviously insufficient to capture the spatial variety of air pollution throughout the city. Although finer resolution products such as the MODIS AOD at 3 km (Remer et al., 2013) and VIIRS AOD at 750 m (Jackson et al., 2013) have also been released, some significant problems, including larger uncertainty in the algorithm accuracy and difficulties in the retrieval over urban surfaces, limit their applications in the urban scale study (Munchak et al., 2013; Huang et al., 2016). In addition, there have been many studies which utilized the 1 km resolution MODIS AOD derived from Multi-Angle Implementation of Atmospheric Correction (MAIAC) algorithm to investigate the spatial distribution, scale and variety of aerosol particle concentration at regional scale (Chudnovsky et al., 2013; Alexeeff et al., 2015; Just et al., 2015; Lee et al., 2016; Sever et al., 2017). Though not available over the entire China at present, the high resolution MAIAC AOD data are beginning to be applied in estimating ground PM2.5 concentration over mega cities of China including Beijing and Shanghai (Liang et al., 2017; Xiao et al., 2017). With the rapid growth of urbanization and industrialization in recent years, air pollution has become an increasingly serious environmental problem in China (Song et al., 2017). High $PM_{2.5}$ concentration and heavy haze pollution were reported to frequently occur in mega cities of China (Tao et al., 2012; Rohde and Muller, 2015). To better understand the air pollution in urban scale, high resolution AOD products covering all land surface types (especially urban areas) are in strong demand all the time.

In this paper, we provide a fresh perspective on the air quality over Wuhan city by taking advantage of a high resolution AOD dataset from our previous work (Sun et al., 2017). The AOD dataset, derived from Wide-Field-of-View (WFV) Camera data onboard Chinese Gaofen-1 (GF-1) satellite, has a spatial resolution of 160 m × 160 m and a re-visiting period of 4 days. GF-1 WFV AOD covers all land surfaces including urban areas in Wuhan, and shows good consistency with MODIS AOD product and ground measurements (Sun et al., 2017). These advantages make it suitable to be applied in the evaluation of air quality over Wuhan. Utilizing the GF-1 WFV AOD dataset from 2013 to 2016, we analyzed the spatial distribution characteristics of AOD over Wuhan, including the AOD map on clean and polluted days, the annual and seasonal variation, and the highly polluted regions. The impacts of land cover types and road density on the spatial distribution of AOD over Wuhan were also discussed. These findings presented in the paper would promote the understanding of air quality in city scale.

2. Study area

Wuhan (113°41′E–115°05′E, 29°58′N–31°22′N), situated on the middle-lower Yangtze Plain and eastern Jianghan Plain, is provincial capital of Hubei province and the largest city in central China, with a population of more than ten million and a covering area of approximately 8594 km^2 (Fig. 1). The city is divided into thirteen districts, which are Caidian, Qiaokou, Dongxihu, Hannan, Hanyang, Hongshan, Huangpi, Jiangan, Jianghan, Jiangxia, Qingshan, Wuchang, and Xinzhou respectively. Seven districts located in the central section (Qiaokou, Hanyang, Hongshan, Jiangan, Jianghan, Qingshan, and Wuchang) constitute the core urban region of Wuhan city (highlighted by red line in Fig. 1). The air pollution over Wuhan has become increasingly serious under the background of rapid development of urbanization and industrialization in recent years. The annual mean AOD at 500 nm was found to be relatively high (up to 1.0) over Wuhan in the last few years (Wang et al., 2015). Wuhan was also identified as a significant region with high aerosol loading in some national scale studies (He et al., 2016b; Sun and Chen, 2017).

3. Material and methods

3.1. GF-1 WFV AOD data

The AOD data used in the study were obtained from our previous work, in which we developed an operational AOD retrieval algorithm for the WFV camera data onboard GF-1 satellite (Sun et al., 2017). The time range of GF-1 WFV AOD is from July 2013 to December 2016, corresponding to all the valid GF-1 satellite data up to 2016. The temporal distribution of valid GF-1 WFV AOD retrievals from 2013 to 2016 is shown in Table 1. There are about 40 days with valid AOD retrievals per year in average. The GF-1 WFV AOD was retrieved by an improved deep blue method similar to the algorithm adopted by MODIS AOD product, which made it possible to cover all land surfaces including urban areas over Wuhan, as well as high spatial resolution (160 m × 160 m) and temporal resolution (4 days). The proposed algorithm utilized the high reflectivity by cloud and high contrast between clouds and the underlying surface to screen clouds. The detailed criterion is: if $\rho_{red}^{TOA} > 0.2$ *and* $\rho_{red}^{TOA} - \rho_{red}^{surface} > 0.1$ then mask. Generally, the method shows a reasonable performance in the cloud mask of GF-1 WFV data. Although in some cases the looser thresholds may result in some extremely high AOD values which actually are retained clouds, the impact of clouds can be minimized in the statistical analysis. Validation results showed that GF-1 WFV AOD had a good consistency with spatio-temporally collocated MODIS AOD (R^2 = 0.66; RMSE = 0.27) and in-situ sun photometer measurements (R^2 = 0.80; RMSE = 0.25). It demonstrates the availability of GF-1 WFV AOD in the evaluation of air quality over Wuhan.

3.2. GF-1 WFV classification data

To analyze the GF-1 WFV AOD over different land use types in Wuhan, a land use map derived from GF-1 WFV imagery was used in the study (Fig. S1). The GF-1 WFV imagery at 16 m resolution was classified using eCognition software, an object-oriented image classification tool designed for high resolution satellite data. The imagery was classified as five types: farmland, urban area, forest, barren land, and water, and they accounted for 24.0%, 23.3%, 20.4%, 17.2%, and 15.0% of the total area respectively. The overall accuracy of the classified results reached to 93.45% in the validation.

3.3. Ground-measured $PM_{2.5}$ data

Hourly ground-measured $PM_{2.5}$ data at 10 monitoring sites in Wuhan from 2013 to 2016 were collected from China Environmental Monitoring Center (CEMC; http://www.cnemc.cn). The ground level $PM_{2.5}$ concentrations were acquired by Tapered Element Oscillating Microbalance (TEOM) method with an accuracy of ± 1.50 μg/m^3 (Wang et al., 2010). Daily average $PM_{2.5}$ were first calculated based on the hourly data from all sites, then annual and seasonal mean $PM_{2.5}$ over Wuhan were obtained to validate the results derived from satellite data.

3.4. Roadway data

The roadway data over Wuhan were obtained from OpenStreetMap in shapefile type (downloaded September 21, 2016; http://www.openstreetmap.org/). The spatial distribution of the roads over Wuhan can be seen in Fig. S2. To explore the relationship between road density and AOD, total road density was calculated using the line density tool in ArcGIS spatial analyst toolbox at the same spatial resolution with GF-1 WFV AOD data.

3.5. Definition of local AOD

As satellite derived AOD is an indicator of total aerosol loading from

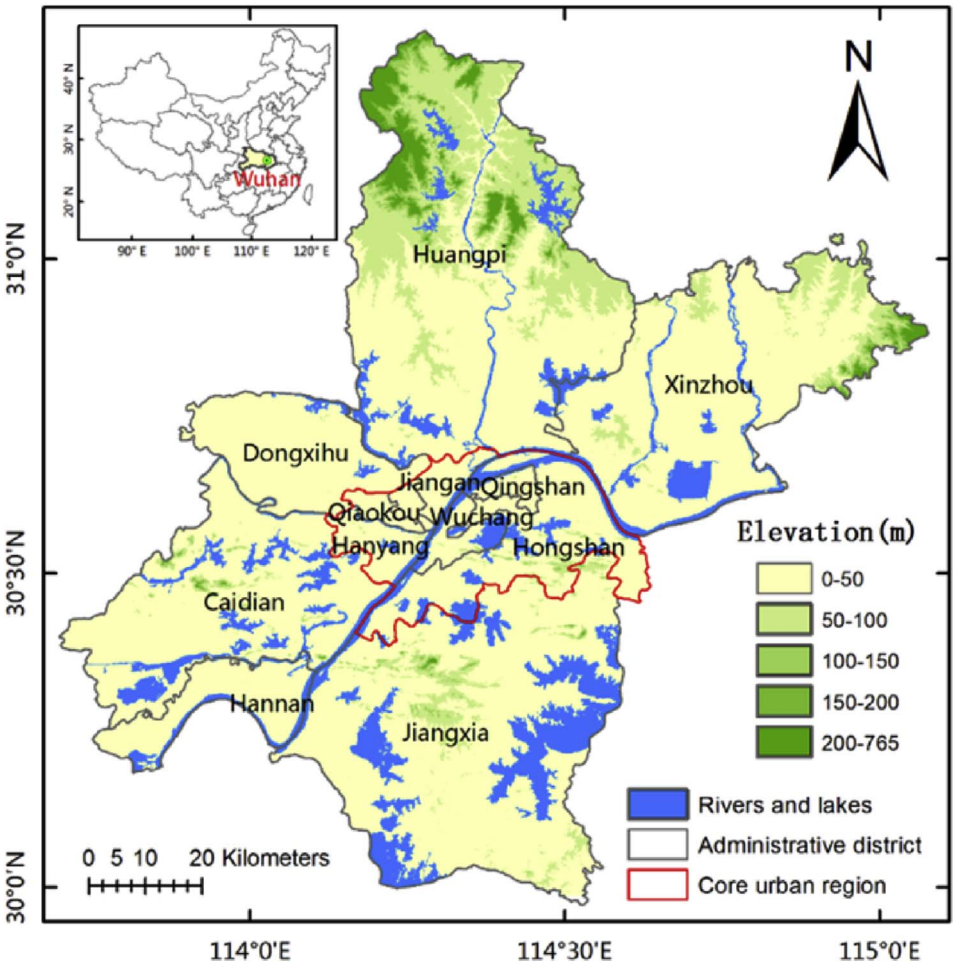

Fig. 1. Geolocation of study area.

Table 1
Temporal distribution of valid GF AOD retrievals over Wuhan during 2013–2016.

Year	Season				Total
	Spring	Summer	Autumn	Winter	
2013	0	7	16	9	32
2014	8	11	9	18	46
2015	9	5	9	8	31
2016	13	16	4	15	48
2013–2016	30	39	38	50	157

both natural and anthropogenic sources, the concept of Local AOD (LAOD), proposed in our previous work (Sun and Chen, 2017), was used to evaluate the localized aerosol loading (aerosols generated from the local region) from anthropogenic sources. LAOD was designed under the assumption of persistent localized aerosol loading over urban areas on both clear and polluted days, and the broad range in the loading of aerosols transported to the local region (close to zero on clear days or huge on polluted days). Although satellite derived AOD is measurement of total aerosol loading from local and transported sources, the lower part of AODs in a certain time series, containing the minimized transported aerosol loading, can be used to indicate the local aerosol loading. Therefore, LAOD is defined as the mean value of AODs whose values are lower than the median value of all valid AODs during a specific period. The design formulas of LAOD can be written as follow:

$$\tau_{med} = Median(\tau_1, \tau_2 \ldots \tau_n);$$

$$\tau_{local} = \sum_{i=1}^{k} \tau_i / k; \ \ where\ \tau_i \le \tau_{med},\ k \ge 5.$$

where $[\tau_1, \tau_2 \ldots \tau_n]$ are all the valid AOD retrievals during one certain period (it can be set as a month, a season or a year); τ_{med} and τ_{local} are the median AOD and LAOD during the period respectively; k is the total number of valid AODs whose values are not greater than τ_{med}, and in order to guarantee the statistical validity, k should be greater than or equal to 5.

The monthly MODIS LAOD has been demonstrated to show a better relationship with ground $PM_{2.5}$ measurements than monthly mean AOD over Wuhan, with a correlation coefficient (R^2) of 0.80/0.66 (Sun and Chen, 2017). It indicates that LAOD is more suitable than mean AOD to represent anthropogenic aerosol loading over Wuhan.

3.6. Definition of urban-induced AOD

Different land use types, associated with various degrees of human activity intensity and diverse aerosol emission sources, may have different influence on the regional air quality. Owing to the concentrated distribution of anthropogenic emissions over urban areas, LAOD over urban areas was found to be obviously higher than LAOD over surrounding non-urban areas. This is a phenomena similar to the well-known urban heat island effect, and it is called urban aerosol effect here, which has been reported by previous study using MODIS AOD at coarse resolution (Gupta et al., 2013). To quantify the impact of urban aerosol effect, the regional mean annual and seasonal LAOD over different land cover types were calculated. Though there are five land use types (forest, urban, farmland, barren land and water) in the classified

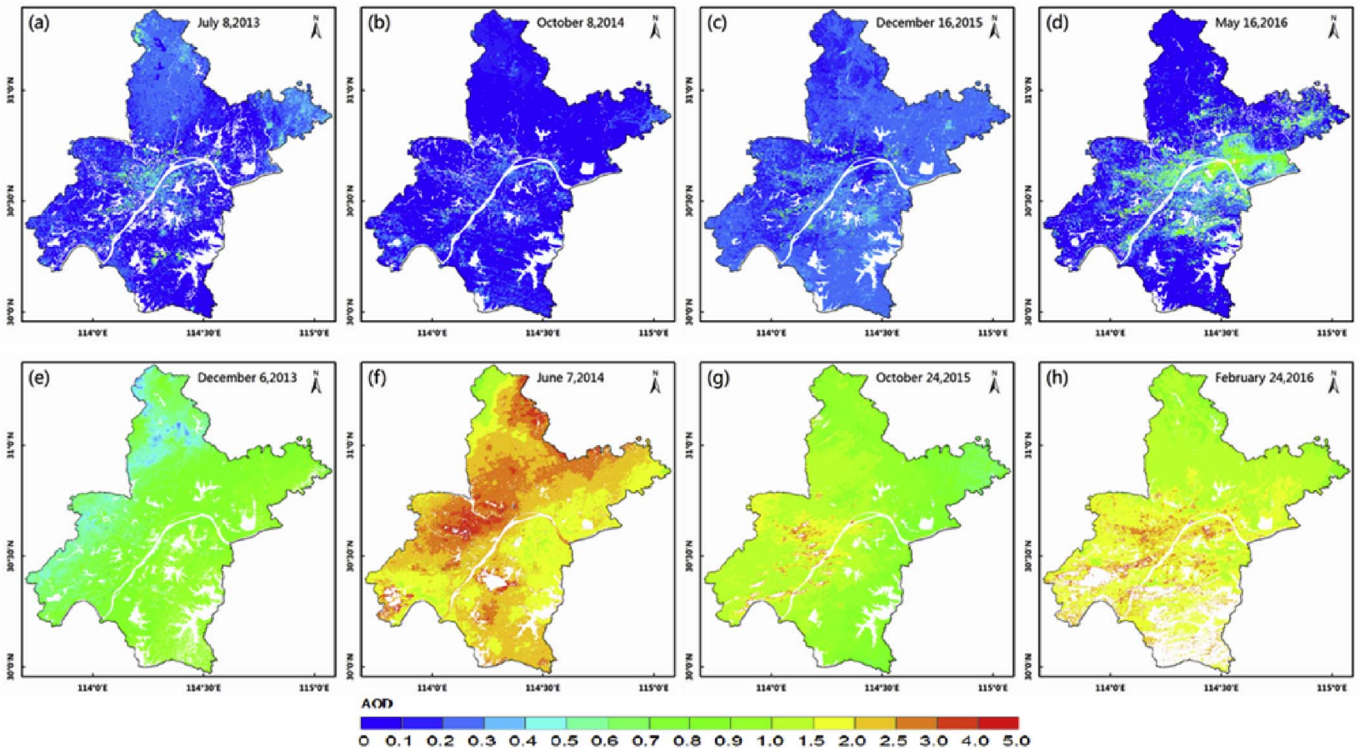

Fig. 2. Spatial distribution of GF-1 WFV AOD in clean (a–d) and polluted (e–h) days.

map (Fig. S1), three land use types (forest, urban, and farmland) were included in the calculation. Water was neglected for lack of valid AOD retrievals; and barren land was merged into farmland. Taking the LAOD over farmland and forest as background, the difference between urban LAOD and background LAOD, defined as urban-induced AOD, can be used to indicate the urban aerosol effect. Urban-induced AOD can be calculated as:

$$\text{Urban} - \text{induced AOD} = LAOD_{urban} - (LAOD_{farmland} + LAOD_{forest})/2.$$

where $LAOD_{urban}$, $LAOD_{farmland}$ and $LAOD_{forest}$ are the regional mean LAOD over land cover types of urban, farmland and forest respectively.

4. Results and discussion

4.1. Spatial distribution of GF-1 WFV AOD over Wuhan

4.1.1. Spatial distribution of GF-1 WFV AOD on clean and polluted days

To explore the spatial distribution of AOD over Wuhan, eight typical GF-1 WFV AOD maps during 2013–2016 were presented in Fig. 2 (cloudless, four on clean days and four on polluted days). The AOD on clean days (shown in Fig. 2a–d) generally ranges from 0 to 0.5, with a uniform spatial distribution over most areas; and the relatively higher AODs are mainly distributed in the core urban region, which clearly reflects the impact of anthropogenic aerosol loading on the local air quality. While on polluted days (shown in Fig. 2e–h) the AOD could exceed 1.0 in most cases, and the higher AODs are no longer concentrated on urban areas. To track the sources of aerosols over Wuhan during the four polluted periods, we conducted a backward trajectory analysis using the NOAA HYSPLIT model (http://ready.arl.noaa.gov/HYSPLIT.php). The back trajectories corresponding to the polluted days (shown in Fig. 2e–h) can be seen in Fig. S3. According to the back trajectories from Fig. S3, the aerosol pollution shown in Fig. 2e–f was transported from North China Plain (NCP). NCP is one of the most polluted areas in China, where heavy haze pollution frequently occurs during recent years (Tao et al., 2012). Aerosol pollution shown in Fig. 2g was transported from the eastern China, which may be caused by biomass burning from agricultural activities; while the aerosol pollution shown in Fig. 2h was transported from the desert areas in northwestern China, indicating that the region was polluted by dust aerosols. In summary, as located in the central China, aerosol pollution over Wuhan could be transported from a variety of sources with different directions.

4.1.2. Spatial distribution of annual local AOD

In order to evaluate the localized aerosol loading from anthropogenic sources, annual and seasonal LAOD was derived using all valid GF-1 WFV AOD retrievals. The annual LAOD maps during 2013–2016 derived from GF-1 WFV AOD retrievals are presented in Fig. 3. Spatially, the distribution of annual LAOD is similar to that of AOD map on clean days (Fig. 2a–d); high LAOD value zone (0.4–0.6) is mainly distributed in the core urban region, where most populations and industries of Wuhan are concentrated. Temporally, the average LAOD over entire Wuhan peaks at 2013 and 2015, with a value of 0.42 and 0.40; the lowest LAOD appears at 2016, with an average value of 0.32. As a comparison, the annual mean AOD was also calculated (Fig. S4). LAOD and mean AOD show a good linear relationship (LAOD = 0.57 × Mean AOD – 0.03), with a correlation coefficient (R^2) of 0.82 (Fig. S5). It indicates the dominant position of localized aerosol loading in total aerosol loading, which has also been reported by previous study using ground measurements (Querol et al., 2006). We also analyzed the spatiotemporal distribution of LAOD in a district view. It is found that the regional mean LAOD of a district generally increases with the increase of its urban cover, following a significantly positive relationship (Fig. 4). The urbanization of a region will usually bring various emission sources including traffic, industry and energy consumption from cooking and heating, which could result in the rise of local aerosol loading and further exacerbate the regional air pollution (Chan and Yao, 2008).

4.1.3. Spatial distribution of seasonal local AOD

Fig. 5 shows the seasonal LAOD map over Wuhan, in which obvious seasonality can be observed. The highest LAOD appears in winter with

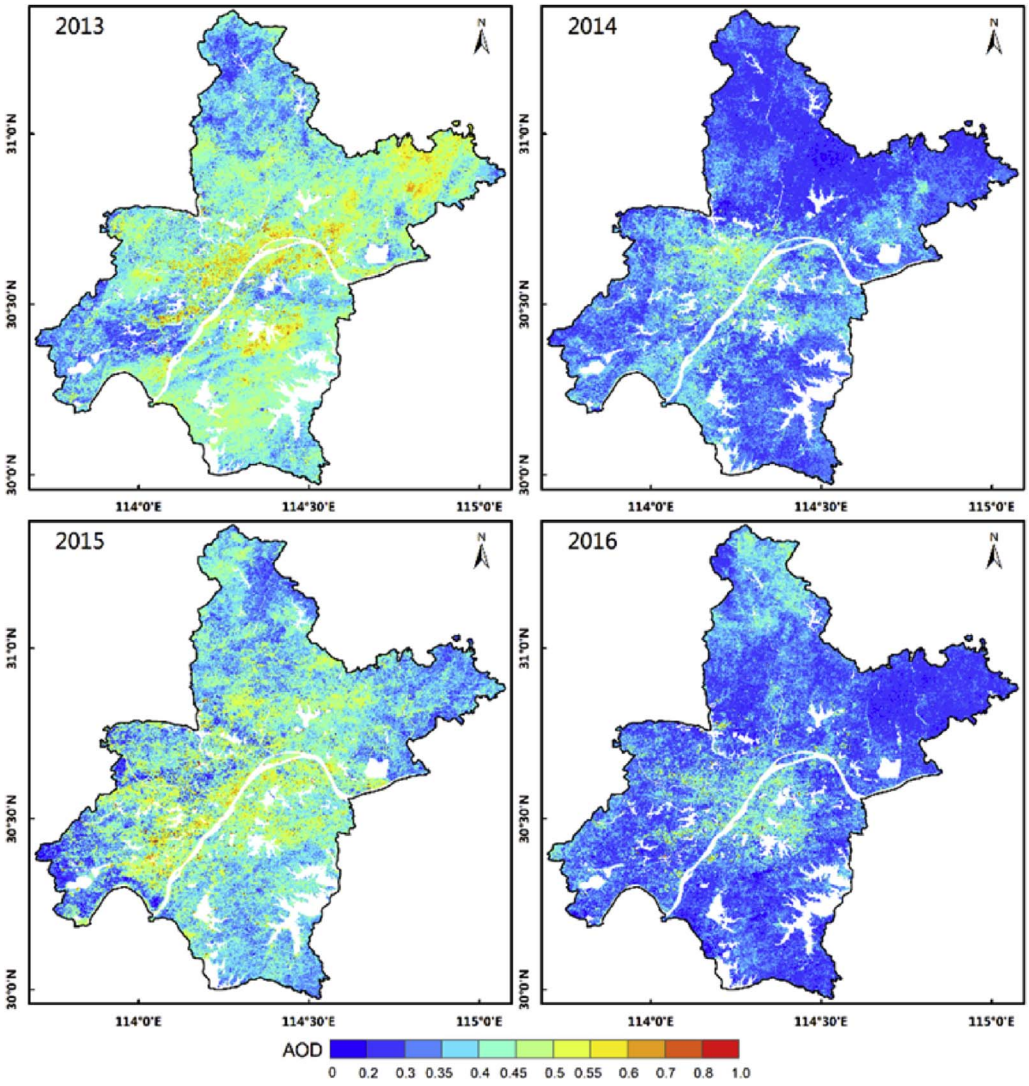

Fig. 3. Spatial distribution of annual local AOD during 2013–2016.

an average value of 0.37, followed by autumn and spring with average value of 0.29 and 0.28. Summer is the cleanest season with an average LAOD of 0.23. In winter, the high LAOD value zone (0.4–0.6) extends from the core urban region in central Wuhan to its surrounding areas. It indicates the existence of massive aerosol loading from local emission, which could be an important factor for the frequently happened haze pollution during this season (Tao et al., 2016). The seasonal variation of LAOD is consistent with the seasonal mean $PM_{2.5}$ derived from ground measurements at the same period (Fig. 6). This seasonality of highest in winter and lowest in summer for aerosol related pollution is the typical pattern at most areas in China (Ma et al., 2016; Song et al., 2017). The relatively higher LAOD in wintertime was a result of enormous local emissions from coal combustion and biomass burning for residential heating and stagnant meteorological conditions that were not

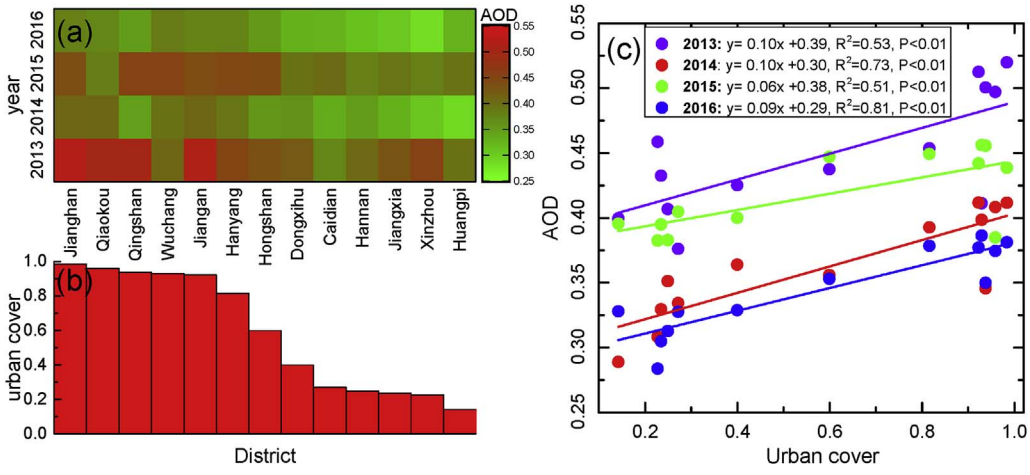

Fig. 4. (a) Regional mean value of annual local AOD over different districts in Wuhan during 2013–2016. (b) Urban cover over different districts in Wuhan. (c) Relationship between annual local AOD and urban cover over different districts in Wuhan. It should be noted here that Fig. 4b has the same x axis with Fig. 4a, and the urban cover of different districts was calculated from land use data shown in Fig. S1.

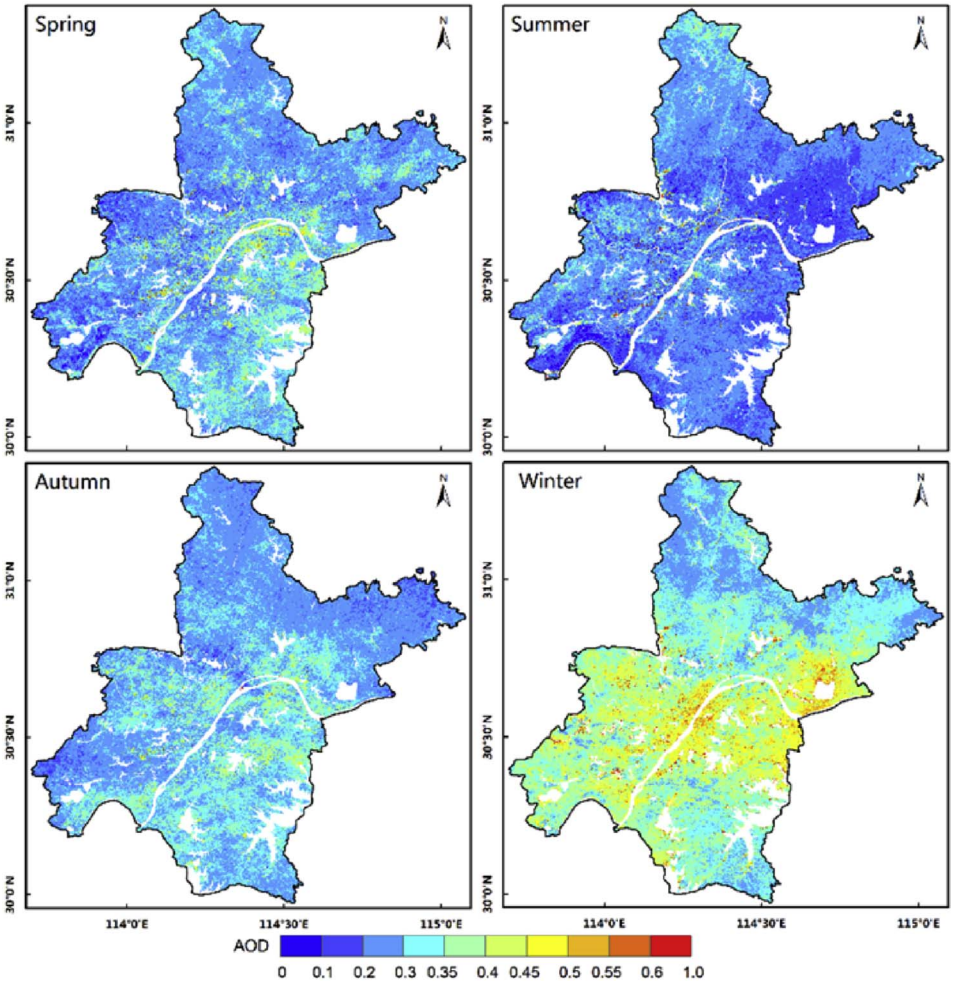

Fig. 5. Spatial distribution of seasonal local AOD during 2013–2016.

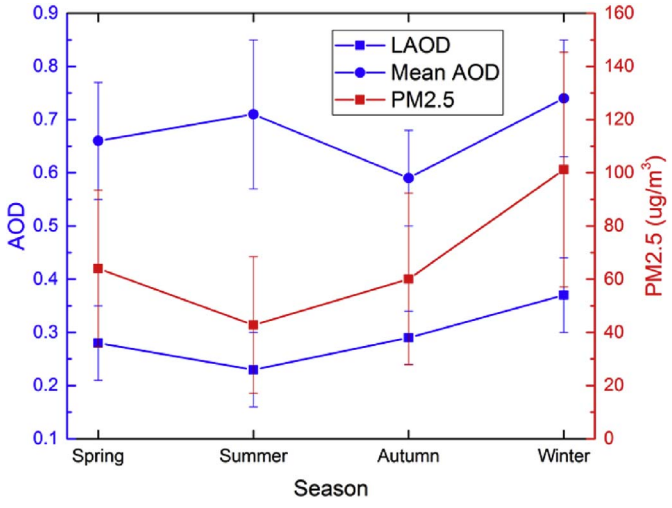

Fig. 6. Seasonal distribution of LAOD, mean AOD and mean $PM_{2.5}$ over Wuhan during 2013–2016.

conducive to the dilution and dispersion of air pollutants. The reduction of local emissions and meteorological conditions beneficial to the dispersion of air pollutants in summertime gave rise to the relatively lower LAOD during this season (Zhang et al., 2011). While the seasonal mean AOD, as shown in Fig. S6 and Fig. 6, is 2–3 times larger than LAOD, and presents a seasonality different from seasonal LAOD and $PM_{2.5}$. Seasonal LAOD shows better relationship with seasonal mean $PM_{2.5}$ than seasonal mean AOD.

4.1.4. Highly polluted regions identified from local AOD map

In addition to the spatiotemporal analysis of annual and seasonal LAOD, the high spatial resolution of GF-1 WFV AOD data makes it possible to locate the detailed local emission sources in this region, which used to be a difficult mission with the frequently-used AOD product (e.g. MODIS). Fig. 7 shows eight typical highly polluted regions identified from the multiyear averaged LAOD map. The detailed information about the selected regions is summarized in Table 2. The main emission sources of each region in the table were determined by referring to the pollution source information from Wuhan Environmental Protection Bureau (http://english.whepb.gov.cn/english/).

The selected highly polluted regions with large local aerosol loadings includes downtown (region A, E in Fig. 7), industrial parks (B, C, G and H), mining area (D), and iron and steel plant (F). Fig. 7 clearly shows the high LAOD value zone (0.4–0.6) distributed over these regions, along with the spatial distribution of the emission sources. It is found that the industrial parks, mainly located in the suburban area of Wuhan, present higher LAOD than other types of polluted regions including downtown areas. The regional mean LAOD of four industrial parks (I, II, III, IV) are 0.473, 0.457, 0.436, and 0.439, which are 33.7%, 29.2%, 23.3%, and 24.1% higher than the mean LAOD over the entire Wuhan respectively. It indicates that there exits persistent and massive emissions from industrial activities over these regions all the year round, which could be the most important source of air pollution over Wuhan. Likewise, high LAOD value is found over downtown areas (0.44 in average, 24–25% higher than mean LAOD over Wuhan), where traffic is the main emission source. The LAOD over downtown areas is

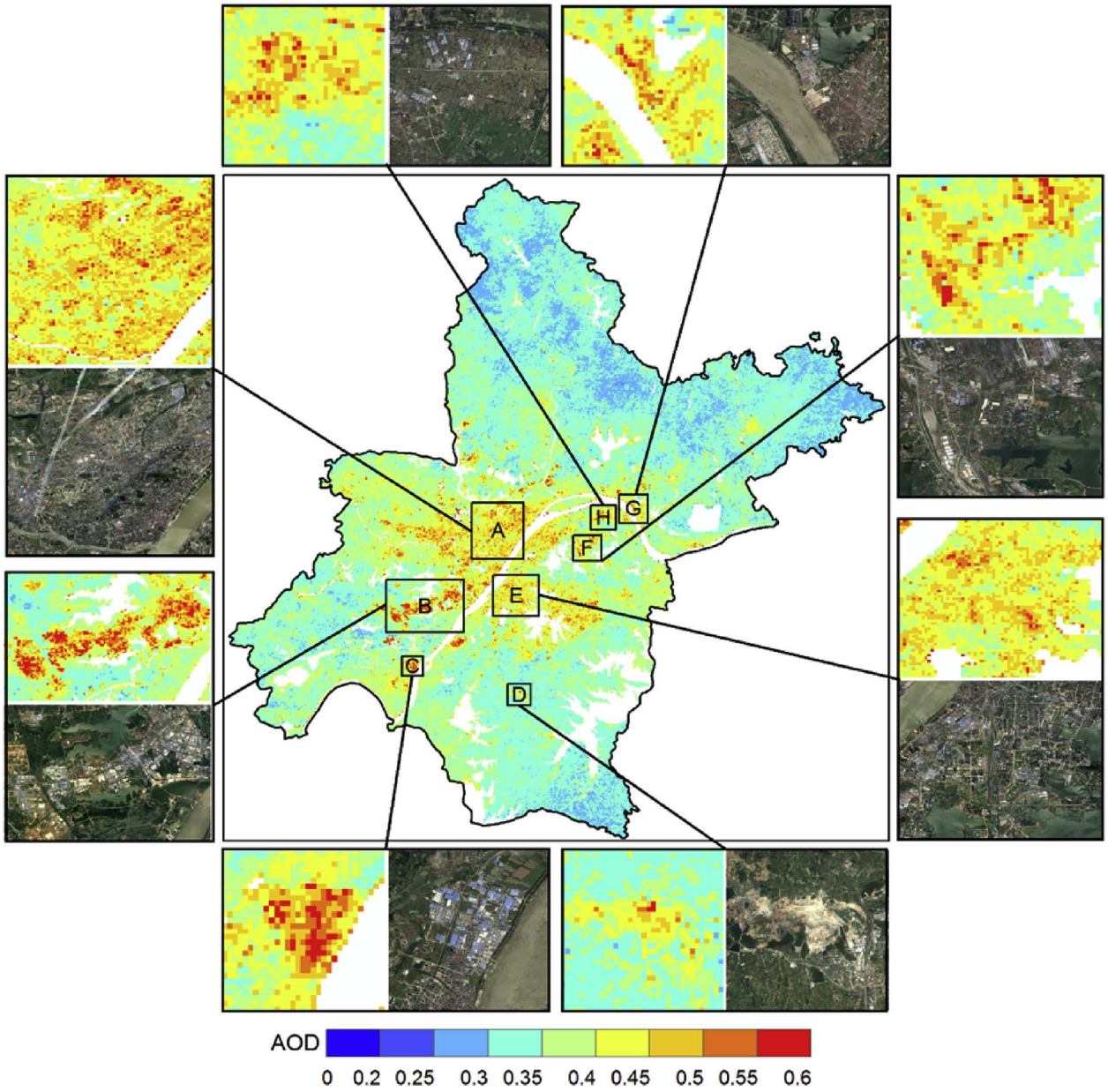

Fig. 7. Highly polluted regions on the multiyear averaged LAOD map. The detailed LAOD map of the polluted regions and corresponding Google Earth images are also presented.

at the same level with LAOD over industrial park III and IV. Some other emission sources from mining, iron and steel industries, could also be clearly identified from the LAOD map (region D, and F in Fig. 7). Their impact could not be neglected in the evaluation of air quality over Wuhan.

Table 2
Summarized information of the highly polluted regions.

Region	Location description	Main emission sources	LAOD (ave ± std)	Higher than average (%)
A	Downtown area I	Traffic	0.443 ± 0.058	25.2
B	Industrial parks I	Diverse industries	0.473 ± 0.077	33.7
C	Industrial parks II	Construction materials industry	0.457 ± 0.078	29.2
D	Mining area	Mining industry	0.396 ± 0.047	12.0
E	Downtown area II	Traffic	0.438 ± 0.039	23.8
F	Iron and steel plant	Iron and steel industry	0.441 ± 0.054	24.7
G	Industrial parks III	Petrochemical and cement industry	0.436 ± 0.049	23.3
H	Industrial parks IV	Diverse industries	0.439 ± 0.045	24.1

Ave ± std represents average value ± standard deviation.
The item of "Higher than average (%)" is calculated as: $(LAOD_{region} - LAOD_{Wuhan})/LAOD_{Wuhan}$. Where $LAOD_{region}$ is the regional mean LAOD over the selected highly polluted regions; and $LAOD_{Wuhan}$ is the regional mean LAOD over the entire Wuhan.

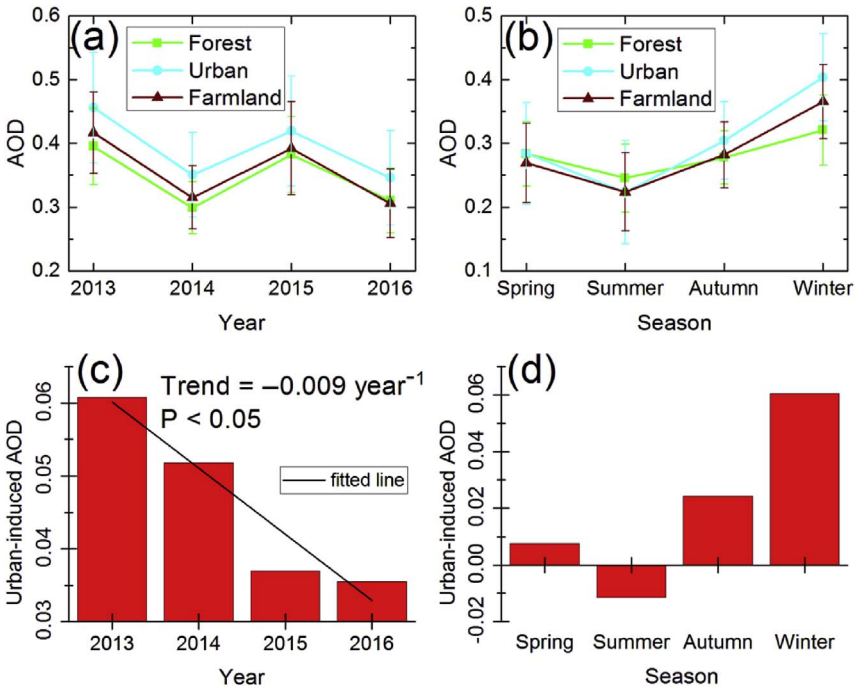

Fig. 8. (a) Annual LAOD over different land use types; (b) Seasonal LAOD over different land use types; (c) Annual distribution of urban-induced AOD; (d) Seasonal distribution of urban-induced AOD.

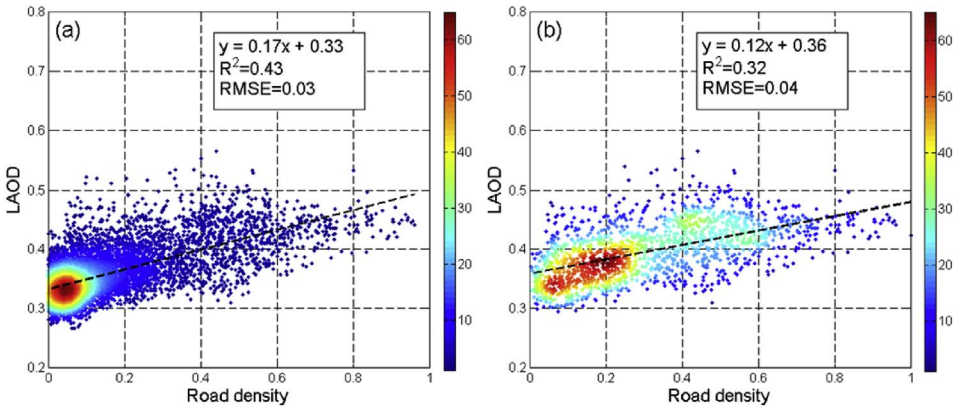

Fig. 9. Relationship between multiyear averaged LAOD and road density over entire region (a) and urban areas (b) of Wuhan. The color bars in the figure represent the point density.

4.2. Annual and seasonal LAOD over different land cover types

Regional mean annual and seasonal LAOD over different land cover types of Wuhan were calculated to explore the relationship between regional LAOD and corresponding land cover types (shown in Fig. 8a–d). It can be clearly seen from Fig. 8a and b that urban LAOD is obviously higher than LAOD over the other two land use types during all years and most seasons (spring, autumn and winter); while annual and seasonal LAOD over farmland is slightly higher than that over forest. The result demonstrates the massive aerosol loading from anthropogenic sources over urban areas in Wuhan. The annual and seasonal distribution of urban-induced AOD can be seen in Fig. 8c and d. Unlike the fluctuation of annual urban LAOD, annual urban-induced AOD changes from 0.061 in 2013 to 0.036 in 2016, presenting a significant downward trend (-0.009 year^{-1}, $P < .05$). The result is consistent with the change trend of annual mean $PM_{2.5}$ over Wuhan (-9.89μg/m^3 year^{-1}, $P < .01$, shown in Fig. S7). It is a reasonable response to the increasingly strict environment policies adopted by local government in recent years (Wang et al., 2017). Similar to seasonal LAOD, urban-induced AOD is highest in winter (0.06), followed by autumn (0.024) and spring (0.008). The urban-induced AOD in summer shows a negative value (-0.01), which may be attributed to the limited satellite sampling period and increasing biomass burning in forest and farmland during this season.

4.3. Relationship between LAOD and road density

On-road vehicle emission is a major source of urban air pollution in many Chinese mega cities (Lang et al., 2014; He et al., 2016a). As a key indicator of vehicle emission, road density has been reported to be spatially consistent with the satellite derived $PM_{2.5}$ in some degree (Xie et al., 2015). To understand the potential of LAOD on reflecting the vehicle emission, here we examined the relationship between LAOD and road density over Wuhan. In the comparison, only road types (primary, secondary, tertiary, trunk and motorway) strongly correlated to vehicle emissions were included in the calculation of road density; road density was normalized to the range of 0–1; and both LAOD and road density were re-gridded to a resolution of 1 × 1 km. The scatter plots between LAOD and road density over entire region and urban areas of Wuhan can be seen in Fig. 9a and b. Significant positive correlations were found over entire Wuhan ($R^2 = 0.43$, slope = 0.17) and its urban areas ($R^2 = 0.32$, slope = 0.12). It indicates that areas with higher road density tends to have higher LAOD. Therefore, satellite derived AOD may be a useful data source in the large-scale estimation of vehicle emissions.

4.4. Outlook of high resolution AOD data in the assessment of urban air pollution

High resolution satellite derived AOD data are very crucial for atmospheric environment assessment at urban scale. Taking advantage of the high spatial and temporal resolution of GF-1 WFV AOD data, we analyzed the spatiotemporal distribution of AOD from local sources over Wuhan. The high spatial resolution of GF-1 WFV AOD made it possible to analyze local AOD in the view of different districts and land cover types, and locate the highly polluted region. Apart from the analysis conducted in this research, a significant application of high resolution AOD data is to estimate the spatial distribution of $PM_{2.5}$. There have been many studies which used high resolution MODIS AOD retrievals to estimate ground-level $PM_{2.5}$ concentrations over different regions (Hu et al., 2014; Alexeeff et al., 2015; Just et al., 2015; Lin et al., 2015; Lee et al., 2016). High resolution AOD data were also used to explore the spatial scales of regional air pollution in some studies (Chudnovsky et al., 2013; Sever et al., 2017). The GF-1 WFV AOD data used in this study, with higher spatial resolution than 1 km MODIS AOD retrievals, could also be applied in such applications in the further research.

5. Conclusion

Unlike the previous analysis of urban air pollution based on ground measurements and models (Querol et al., 2006; He et al., 2016a; Song et al., 2017), this study provided a satellite view of air pollution in urban scale using the high resolution AOD dataset. Satellite derived AOD clearly presented the persistent aerosol concentrations over urban areas on clean days, and severe aerosol pollution transported from different sources and directions on polluted days. Therefore, the concept of LAOD (Sun and Chen, 2017) was adopted to estimate the local contributions to aerosol concentrations from satellite derived AOD. By analyzing the annual and seasonal LAOD over Wuhan, we found that districts with higher urban cover tended to have higher LAOD, which revealed the impact of urbanization on the local air pollution. In accordance with the seasonal mean $PM_{2.5}$, seasonal LAOD over Wuhan presented a seasonality of highest in winter and lowest in summer, which was also the typical pattern at most areas of China.

The influence of different emission sources on the regional air quality was investigated by analysis of highly polluted regions identified from the LAOD map. It was found that industrial parks showed the highest LAOD when compared with other types of polluted regions. It demonstrated that industrial emission could be the major source of air pollution over Wuhan. Allowing for the difference of LAOD between urban areas and other land types, urban-induced AOD was defined to quantify the urban aerosol effect (similar to the urban heat island effect). Annually, urban-induced AOD shows a significant downward trend ($-0.009\ year^{-1}$, $P < .05$), which is consistent with the change trend of $PM_{2.5}$ over Wuhan ($-9.89 \mu g/m^3\ year^{-1}$, $P < .01$). It is a reasonable response to the stricter environment policies adopted by local government in recent years. Seasonally, the highest urban-induced AOD appears in winter with a value of 0.06, which is much greater than other seasons. It indicates the existence of massive local emissions, which could partly explain the frequently happened haze pollution during this season. LAOD was also found to have a reasonable relationship with road density in Wuhan ($R^2 = 0.43$, slope = 0.17). In summary, our work provide some new perspectives on the air quality in Wuhan using GF-1 WFV AOD data. The application potential of high resolution satellite derived AOD in the evaluation of urban air quality is obvious upon our research.

Acknowledgments

This work was supported by the National Key Research and Development Program of China (Grant No. 2017YFB0503905, 2017YFC0212600, 2016YFC0200900), and the National Science Foundation of China (Grant No. 41331174, 41571344). The authors gratefully acknowledge the China Center for Resources Satellite Data and Application (CRESDA) for the provision of GF-1 WFV data, and the NOAA Air Resources Laboratory (ARL) for the HYSPLIT model used in this publication.

Appendix B. Supplementary data

Supplementary data related to this article can be found at http://dx.doi.org/10.1016/j.apr.2017.12.011.

References

Alexeeff, S.E., Schwartz, J., Kloog, I., Chudnovsky, A., Koutrakis, P., Coull, B.A., 2015. Consequences of kriging and land use regression for PM2.5 predictions in epidemiologic analyses: insights into spatial variability using high-resolution satellite data. J. Expo. Sci. Environ. Epidemiol. 25, 138–144.
Chan, C.K., Yao, X., 2008. Air pollution in mega cities in China. Atmos. Environ. 42, 1–42.
Chudnovsky, A., Kostinski, A.B., Lyapustin, A.I., Koutrakis, P., 2013. Spatial scales of pollution from variable resolution satellite imaging. Environ. Pollut. 172, 131–138.
Ginoux, P., Garbuzov, D.Z., Hsu, N.C., 2010. Identification of anthropogenic and natural dust sources using Moderate Resolution Imaging Spectroradiometer (MODIS) Deep Blue level 2 data. J. Geophys. Res. 115.
Gupta, P., Khan, M., Silva, A.D., Patadia, F., 2013. MODIS aerosol optical depth observations over urban areas in Pakistan: quantity and quality of the data for air quality monitoring. Atmos. Pollut. Res. 4, 43–52.
Hao, N., Valks, P., Loyola, D., Cheng, Y.F., Zimmer, W., 2011. Space-based measurements of air quality during the world expo 2010 in Shanghai. Environ. Res. Lett. 6.
Haywood, J., Boucher, O., 2000. Estimates of the direct and indirect radiative forcing due to tropospheric aerosols: a review. Rev. Geophys. 38, 513–543.
He, J., Wu, L., Mao, H., Liu, H., Jing, B., Yu, Y., Ren, P., Feng, C., Liu, X., 2016a. Development of a vehicle emission inventory with high temporal-spatial resolution based on NRT traffic data and its impact on air pollution in Beijing - Part 2: impact of vehicle emission on urban air quality. Atmos. Chem. Phys. 16, 3171–3184.
He, Q., Zhang, M., Huang, B., 2016b. Spatio-temporal variation and impact factors analysis of satellite-based aerosol optical depth over China from 2002 to 2015. Atmos. Environ. 129, 79–90.
Hsu, N.C., Jeong, M.J., Bettenhausen, C., Sayer, A.M., Hansell, R.A., Seftor, C.S., Huang, J., Tsay, S.C., 2013. Enhanced Deep Blue aerosol retrieval algorithm: the second generation. J. Geophys. Res. 118, 9296–9315.
Hu, X., Waller, L.A., Lyapustin, A.I., Wang, Y., Alhamdan, M.Z., Crosson, W.L., Estes, M.G., Estes, S., Quattrochi, D.A., Puttaswamy, S.J., 2014. Estimating ground-level PM (sub 2.5) concentrations in the southeastern United States using MAIAC AOD retrievals and a two-stage model. Rem. Sens. Environ. 140, 220–232.
Huang, J., Kondragunta, S., Laszlo, I., Liu, H., Remer, L.A., Zhang, H., Superczynski, S., Ciren, P., Holben, B.N., Petrenko, M.V., 2016. Validation and expected error estimation of suomi-NPP VIIRS aerosol optical thickness and ångström exponent with AERONET. J. Geophys. Res.
Huang, R., Zhang, Y., Bozzetti, C., Ho, K., Cao, J., Han, Y., Daellenbach, K.R., Slowik, J.G., Platt, S.M., Canonaco, F., 2014. High secondary aerosol contribution to particulate pollution during haze events in China. Nature 514, 218.
Jackson, J.M., Liu, H., Laszlo, I., Kondragunta, S., Remer, L.A., Huang, J., Huang, H., 2013. Suomi-NPP VIIRS aerosol algorithms and data products. J. Geophys. Res. 118.
Just, A.C., Wright, R.O., Schwartz, J., Coull, B.A., Baccarelli, A., Tellezrojo, M.M., Moody, E., Wang, Y., Lyapustin, A.I., Kloog, I., 2015. Using high-resolution satellite aerosol optical depth to estimate daily PM2.5 geographical distribution in Mexico City. Environ. Sci. Technol. 49, 8576–8584.
Kahn, R.A., Gaitley, B.J., Garay, M.J., Diner, D.J., Eck, T.F., Smirnov, A., Holben, B.N., 2010. Multiangle imaging SpectroRadiometer global aerosol product assessment by comparison with the aerosol robotic network. J. Geophys. Res. 115.
Kaufman, Y.J., Tanré, D., Boucher, O., 2002. A satellite view of aerosols in the climate system. Nature 419, 215–223.
Lang, J., Cheng, S., Zhou, Y., Zhang, Y., Wang, G., 2014. Air pollutant emissions from on-road vehicles in China, 1999-2011. Sci. Total Environ. 496, 1–10.
Lee, M., Kloog, I., Chudnovsky, A., Lyapustin, A.I., Wang, Y., Melly, S.J., Coull, B.A., Koutrakis, P., Schwartz, J., 2016. Spatiotemporal prediction of fine particulate matter using high-resolution satellite images in the Southeastern US 2003-2011. J. Expo. Sci. Environ. Epidemiol. 26, 377–384.
Levy, R.C., Mattoo, S., Munchak, L.A., Remer, L.A., Sayer, A.M., Patadia, F., Hsu, N.C., 2013. The Collection 6 MODIS aerosol products over land and ocean. Atmos. Meas. Tech. 6, 2989–3034.
Liang, F., Xiao, Q., Wang, Y., Lyapustin, A., Li, G., Gu, D., Pan, X., Liu, Y., 2017. MAIAC-based long-term spatiotemporal trends of PM2.5 in Beijing, China. Sci. Total Environ. 616-617, 1589–1598.
Lin, C., Li, Y., Yuan, Z., Lau, A.K., Li, C., Fung, J.C.H., 2015. Using satellite remote sensing data to estimate the high-resolution distribution of ground-level PM2.5. Rem. Sens. Environ. 156, 117–128.
Ma, Z.W., Hu, X.F., Sayer, A.M., Levy, R., Zhang, Q., Xue, Y.G., Tong, S.L., Bi, J., Huang, L., Liu, Y., 2016. Satellite-based spatiotemporal trends in PM2.5 concentrations: China, 2004-2013. Environ. Health Perspect. 124, 184–192.

Mishchenko, M.I., Geogdzhayev, I.V., Cairns, B., Carlson, B.E., Chowdhary, J., Lacis, A.A., Liu, L., Rossow, W.B., Travis, L.D., 2007. Past, present, and future of global aerosol climatologies derived from satellite observations: a perspective. J. Quant. Spectrosc. Radiat. Transf. 106, 325–347.

Mishchenko, M.I., Geogdzhayev, I.V., Liu, L., Ogren, J.A., Lacis, A.A., Rossow, W.B., Hovenier, J.W., Volten, H., Munoz, O., 2003. Aerosol retrievals from AVHRR radiances: effects of particle nonsphericity and absorption and an updated long-term global climatology of aerosol properties. J. Quant. Spectrosc. Radiat. Transf. 79, 953–972.

Munchak, L.A., Levy, R.C., Mattoo, S., Remer, L.A., Holben, B.N., Schafer, J.S., Hostetler, C.A., Ferrare, R.A., 2013. MODIS 3 km aerosol product: applications over land in an urban/suburban region. Atmos. Meas. Tech. 6, 1747–1759.

Querol, X., Zhuang, X., Alastuey, A., Viana, M., Lv, W., Wang, Y., Lopez, A., Zhu, Z., Wei, H., Xu, S., 2006. Speciation and sources of atmospheric aerosols in a highly industrialised emerging mega-city in Central China. J. Environ. Monit. 8, 1049–1059.

Remer, L.A., Mattoo, S., Levy, R.C., Munchak, L.A., 2013. MODIS 3 km aerosol product: algorithm and global perspective. Atmos. Meas. Tech. 6, 1829–1844.

Rohde, R.A., Muller, R.A., 2015. Air pollution in China: mapping of concentrations and sources. PLos One 10.

Sever, L., Alpert, P., Lyapustin, A., Wang, Y., Chudnovsky, A., 2017. An example of aerosol pattern variability over bright surface using high resolution MODIS MAIAC: the eastern and western areas of the Dead Sea and environs. Atmos. Environ. 165, 359–369.

Song, C., Wu, L., Xie, Y., He, J., Chen, X., Wang, T., Lin, Y., Jin, T., Wang, A., Liu, Y., Dai, Q., Liu, B., Wang, Y., Mao, H., 2017. Air pollution in China: status and spatiotemporal variations. Environ. Pollut. 227, 334–347.

Sorekhamer, M., Strawa, A.W., Chatfield, R.B., Esswein, R.F., Cohen, A., Broday, D.M., 2013. Improved retrieval of PM2.5 from satellite data products using non-linear methods. Environ. Pollut. 182, 417–423.

Stocker, T., 2014. Climate Change 2013: the Physical Science Basis : Working Group I Contribution to the Fifth Assessment Report of the Intergovernmental Panel on Climate Change. Cambridge University Press, New York.

Sun, K., Chen, X., 2017. Spatio-temporal distribution of localized aerosol loading in China: a satellite view. Atmos. Environ. 163, 35–43.

Sun, K., Chen, X., Zhu, Z., Zhang, T., 2017. High resolution aerosol optical depth retrieval using Gaofen-1 WFV camera data. Rem. Sens. 9, 89.

Tao, M., Chen, L., Su, L., Tao, J., 2012. Satellite observation of regional haze pollution over the North China Plain. J. Geophys. Res.-Atmos. 117.

Tao, M., Chen, L., Wang, Z., Wang, J., Tao, J., Wang, X., 2016. Did the widespread haze pollution over China increase during the last decade? A satellite view from space. Environ. Res. Lett. 11.

Torres, O., Bhartia, P.K., Herman, J.R., Sinyuk, A., Ginoux, P., Holben, B.N., 2002. A long-term record of aerosol optical depth from TOMS observations and comparison to AERONET measurements. J. Atmos. Sci. 59, 398–413.

Van Donkelaar, A., Martin, R.V., Brauer, M., Hsu, N.C., Kahn, R.A., Levy, R.C., Lyapustin, A., Sayer, A.M., Winker, D.M., 2016. Global estimates of fine particulate matter using a combined geophysical-statistical method with information from satellites, models, and monitors. Environ. Sci. Technol. 50, 3762–3772.

Wang, K., Dickinson, R.E., Liang, S., 2009. Clear sky visibility has decreased over land globally from 1973 to 2007. Science 323, 1468–1470.

Wang, L., Gong, W., Xia, X., Zhu, J., Li, J., Zhu, Z., 2015. Long-term observations of aerosol optical properties at Wuhan, an urban site in Central China. Atmos. Environ. 101, 94–102.

Wang, P., Liu, L., Wu, T., 2017. A review of China's climate governance: state, market and civil society. Clim. Pol. 1–16.

Wang, Z., Chen, L., Tao, J., Zhang, Y., Su, L., 2010. Satellite-based estimation of regional particulate matter (PM) in Beijing using vertical-and-RH correcting method. Rem. Sens. Environ. 114, 50–63.

Xiao, Q., Wang, Y., Chang, H.H., Meng, X., Geng, G., Lyapustin, A., Liu, Y., 2017. Full-coverage high-resolution daily PM2.5 estimation using MAIAC AOD in the Yangtze River Delta of China. Rem. Sens. Environ. 199, 437–446.

Xie, Y., Wang, Y., Zhang, K., Dong, W., Lv, B., Bai, Y., 2015. Daily estimation of ground-level PM2.5 concentrations over Beijing using 3 km resolution MODIS AOD. Environ. Sci. Technol. 49, 12280–12288.

Yang, J., Gong, P., Fu, R., Zhang, M.H., Chen, J.M., Liang, S.L., Xu, B., Shi, J.C., Dickinson, R., 2014. The role of satellite remote sensing in climate change studies. Nat. Clim. Change 4, 74.

Zhang, X., Wang, Y., Niu, T., Zhang, X., Gong, S.L., Zhang, Y.M., Sun, J.Y., 2011. Atmospheric aerosol compositions in China: spatial/temporal variability, chemical signature, regional haze distribution and comparisons with global aerosols. Atmos. Chem. Phys. 12, 779–799.